Quantification of nano-scale interface structures to guide mechanistic modelling of WC grain coarsening inhibition in V-doped hard metals

(article starts on next page)

Quantification of nano-scale interface structures to guide mechanistic modelling of WC grain coarsening inhibition in V-doped hard metals

Ahmet Bahadir Yildiz [a,*], R. Prasath Babu [a], Manon Bonvalet-Rolland [a], Sebastian Busch [b], Vasyl Ryukhtin [c], Jonathan Weidow [d], Susanne Norgren [e], Peter Hedström [a]

[a] Department of Materials Science and Engineering, KTH Royal Institute of Technology, SE-100 44 Stockholm, Sweden
[b] German Engineering Materials Science Centre (GEMS) at Heinz Maier-Leibnitz Zentrum (MLZ), Helmholtz-Zentrum Geesthacht GmbH, Lichtenbergstrasse 1, 85747 Garching bei München, Germany
[c] Nuclear Physics Institute, 250 68, cp. 130, Husinec-Řež, Czech Republic
[d] Department of Physics, Chalmers University of Technology, SE-412 96 Göteborg, Sweden
[e] Sandvik Coromant R&D, SE-126 80 Stockholm, Sweden

HIGHLIGHTS

- WC/Co interface structure is quantified by Small-angle neutron scattering (SANS).
- Grain coarsening inhibition starts upon atomic segregation of V at WC/Co interface.
- Increasing amounts of V-doping bring enhanced nano-layer coverage on WC grains.
- Mean-field simulations rationalize that two inhibition mechanisms are at play.

GRAPHICAL ABSTRACT
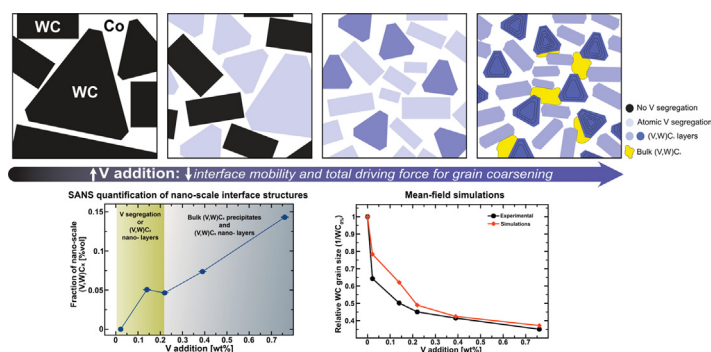
ARTICLE INFO

ABSTRACT

The control of tungsten carbide (WC) grain coarsening using coarsening inhibitors is considered to be one of the most important advancements for hard metals, leading to metal cutting tools with increased performance. Until now, however, the grain coarsening inhibition mechanism for effective inhibitors such as V has been elusive, posing an obstacle to material optimization. This study serves to quantify the presence of nanoscale V-W-C over a wide range of V/Co ratios by small-angle neutron scattering (SANS). The experiments help to delineate how additions of V affect the nanostructure during sintering and result in smaller WC grains. In contrast to the common view that grain coarsening inhibition originates from the presence of stable nanoscale $(V,W)C_x$ complexions formed at the WC/Co interfaces, we show that V segregates at the WC/Co interfaces already upon a minor addition of V and brings significant coarsening inhibition. Increasing additions of V result in the formation of $(V,W)C_x$ complexions; and above 0.76 wt% V addition, where the coverage on WC grains is complete, no further reduction in average grain size is observed. Mechanistic modelling of grain coarsening reveals that grain coarsening inhibition is governed by the reduction of interface mobilities and total driving force for coarsening.

* Corresponding author.
  E-mail address: abyildiz@kth.se (A.B. Yildiz).

1. Introduction

Hard metals, also known as cemented carbides, are composite materials traditionally consisting of hard tungsten carbide (WC) particles bound together by a metallic, often Co-rich, ductile phase. The excellent combination of high hardness, resistance to wear, and toughness has made hard metals the premier choice of material for metal cutting and rock excavation. Efficient machining of complex components, e.g. printed circuit boards and aerospace parts, requires fine-grained hard metal tools with sharp cutting edges [1–3]. For a constant binder phase fraction, the hardness of a hard metal follows the Hall-Petch relation [4] and increases with decreasing WC grain size [5,6]. Furthermore, since abnormally large grains [7,8] are detrimental to the performance of a hard metal by promoting crack initiation [9], a uniform distribution of WC grains is desired in the as-sintered material. Therefore, the control of WC grain coarsening is important and this is achieved using grain coarsening inhibitors such as Cr, Ti, and V [10–13]. V has been suggested to be the most effective addition, inhibiting both the continuous and discontinuous (abnormal) grain coarsening of WC [11,12,14].

Significant efforts have been made to reveal the mechanism(s) behind the effective grain coarsening inhibition of V. The discussions centre around the presence of substoichiometric $(V,W)C_x$ nano-layers, i.e. complexions [15,16], at the WC/Co interface [13,17–26]. These complexions have been suggested to inhibit coarsening by different mechanisms, including retarded diffusion through the WC/Co interface and hindered dissolution and re-precipitation of WC grains [22–24,26]. It has been shown that interfacial $(V,W)C_x$ nano-layers reduce the WC/Co interfacial energy, which makes the formation of such interfacial layers energetically favourable, i.e. stable, at a certain temperature range below the solubility limit of V in the Co-rich binder [25]. Even though atom probe tomography (APT) [20] and transmission electron microscopy (TEM) studies [13,21–24,26] for different V/Co ratios have shown similar WC/Co interface structures, the reported WC grain size values in the literature vary significantly with the V/Co ratio [18,27,28]; and the reason behind such divergence is yet to be understood. One reason behind the inconclusive understanding of the effect of V on grain coarsening is the lack of volume-averaged experimental quantification of the nanostructure formation. Previous work has been limited to TEM and APT, where the limited probed volumes have prevented a complete quantitative view of the nanostructure formation.

Here, we thus utilize nuclear and magnetic small-angle neutron scattering (SANS) to quantify the formation of nanoscale $(V,W)C_x$ features over a wide range of V/Co ratios and report on thermodynamic calculations and mean-field modelling to rationalize the mechanisms of WC grain coarsening inhibition. Whilst TEM-related techniques complement the SANS data by providing information on the WC/Co interface structure in relation to the crystallographic orientation and the morphology of WC grains, electron backscatter diffraction (EBSD) and very-SANS (VSANS) measurements are used to study the microstructural refinement in terms of WC grain size and Co-rich binder pocket size, respectively.

2. Materials and methods

2.1. Synthesis, mechanical property tests and chemical analysis

Five V-doped (0.02, 0.14, 0.22, 0.39, and 0.76 wt%) WC-10.07 wt% Co-V materials and one WC-11.45 wt% Co reference material were produced. The powder mixtures were prepared by milling in WC-Co lined rotating 0.25 L mill in ethanol and 2 wt% polyethylene glycol using 800 g of WC-Co milling bodies for 8 h using WC, VC, and Co powders with average diameters [29] of 0.9 μm, 1.6 μm and 0.9 μm, respectively. The powder mixtures were later on pan-dried and pressed, then debound using H_2 atmosphere at 450 °C; followed by ramping in vacuum to 1410 °C with 8 °C/min heating rate and liquid-phase sintering in controlled vacuum at 1410 °C for 1 h. Finally, the sintered hard metals were cooled to 1250 °C with a cooling rate of 5 °C/min before self-cooled in the furnace to room temperature. The hardness and fracture toughness of the materials were determined by indentations applying 30 kg load as described in Ref. [30]. The chemical composition of the as-sintered samples (Table 1) was determined by: (i) X-ray fluorescence spectrometry using Axios mAX-Advanced PW4400 (Malvern Panalytical) spectrometer for V and Co analysis; (ii) infrared absorption spectrometry using Leco CS-844 determinator for C analysis; and, (iii) inductively coupled plasma - optical emission spectrometry (ICP-OES) using Spectro Arcos SOP 130 for trace analysis of V in 0% and 0.02% V samples. The similar carbon contents and the use of the same initial powders, powder processing, and sintering conditions ensure that the level of V addition is the only parameter affecting the structure evolution.

2.2. Electron microscopy

A probe Cs corrected FEI Titan Themis TEM equipped with energy dispersive x-ray spectroscopy Super-X EDX, operated at 200 kV was used for microstructural, chemical and diffraction investigations. TEM thin foil samples from WC-Co-V bulk samples were prepared by *in-situ* lift out with a dual-beam FIB-SEM (FEI Nova600 workstation) with a Ga liquid–metal ion source. Scanning-TEM (STEM) bright field (BF) was utilized for imaging. Selected area electron diffraction (SAED) was used to identify the orientation and tilt the sample such that the WC crystals have the interface of interest oriented parallel to the beam direction. TEM imaging and analysis (TIA) software interface was utilized to acquire images and EDX point analysis data, while Bruker Esprit 1.9 user interface was used to acquire and analyse the EDX spectral maps. In EDX quantitative calculations, C signal from the spectrum was not considered, since there is high ambiguity due to contamination in the TEM chamber and sample.

EBSD measurements were carried out using 50 nm step size in a Tescan GAIA3 FIB-SEM operated at 20 kV acceleration voltage equipped with an Oxford Instruments NordlysNano camera. The mechanically polished sintered samples were finally polished by Ar^+ for two hours in a Gatan Precision Ion Polishing System Model 691 prior to EBSD measurements. Grains were defined as regions>3 pixels and a misorientation threshold angle of > 3° was used. Whilst AZtecHKL and Tango software packages (Oxford Instruments, UK) were used for the post-processing and analyses, coloured EBSD maps of WC grains were created in the software package MTEX [31].

2.3. SANS and V-SANS

SANS experiments were performed on the SANS-1 beamline at the Heinz Maier-Leibnitz Zentrum (MLZ), Garching, Germany [32] using a neutron wavelength of 4.5 Å ($\Delta\lambda/\lambda$ = 10%) at two sample-to-detector distances: 2 m and 8 m, and at 8 m and 12 m collimation lengths, respectively. This experimental setup spanned a scattering vector (Q) range of 0.0076–0.38 Å^{-1} ($Q = (4\pi/\lambda)\sin\theta$, where θ is half of the scattering angle). To reduce the probability of multiple scattering, the specimen thickness was limited to 0.2 mm at which ~ 90% transmission was observed. Square specimens with a dimension of 12 mm × 12 mm were used, resulting in about 13 mm^3 probed volume. A magnetic field of 2 T was applied at the sample position perpendicular to the neutron beam, allowing

Table 1

Chemical composition of the as-sintered samples in wt%.

Sample*	V	C	Co	W
0% V	<0.002	5.43	11.30	Bal.
0.02%	0.021	5.48	9.99	Bal.
0.14%	0.12	5.50	10.00	Bal.
0.22%	0.19	5.51	9.97	Bal.
0.39%	0.32	5.52	10.00	Bal.
0.76%	0.64	5.55	10.10	Bal.

*Sample names represent the powder mixture composition prior the sintering.

the separation of nuclear and magnetic scattering signals. The reduction and correction of the raw SANS data were performed using the BerSANS software [33]. The measured SANS intensities were corrected for the electronic background using B_4C, normalized by the transmission, scaled to the absolute units $d\Sigma/d\Omega$ [cm^{-1}] using H_2O standard and the probe volume, and finally nuclear and magnetic scattering contributions were deconvoluted.

The nuclear scattering length density (SLD) of $(V,W)C_x$ (3.78×10^{-6} $Å^{-2}$) lies between that of pure Co (2.26×10^{-6} $Å^{-2}$) and WC (5.48×10^{-6} $Å^{-2}$) [28]. Therefore, at the same size range with $(V,W)C_x$ precipitates, the scattering originates mainly from the Co-rich binder pockets due to (i) the higher scattering length density difference $\Delta\rho$ between WC and pure Co; and, (ii) the higher volume fraction of Co-rich binder compared to that of $(V,W)C_x$. This makes the separation of scattering contribution of $(V,W)C_x$ precipitates infeasible by using nuclear SANS data alone. At that point, magnetic SANS data, which solely provides information on the scattering of ferromagnetic Co-rich binder pockets, becomes a useful tool. Thus, to separate the scattering caused by binder pockets, the term $I(Q)_{Co,MAG}$ describing the magnetic scattering of Co-rich binder pockets was determined by extracting the power law scattering from the experimental magnetic scattering cross-section $(d\Sigma/d\Omega)_{MAG}$ in Irena tool suite [34]. The magnetic $\Delta\rho$ between pure Co (4.29×10^{-6} $Å^{-2}$) and vacuum is different than the nuclear $\Delta\rho$ between pure Co and WC (3.22×10^{-6} $Å^{-2}$). Since the scattering contribution evolves with the square of $\Delta\rho$, the residual scattering contribution $I(Q)_{Co,MAG}$ was normalized, i.e. $I(Q)_{Co,MAG} = 1.77 \times I(Q)_{Co,NUC}$, and used as background BKG contribution in the nuclear scattering pattern. BKG includes two additional nuclear scattering contributions: (i) the power law scattering, BQ^{-P}, originating from the larger scatterers, e.g. WC in the current study; B is the scaling factor and P is the slope of the power law; and (ii) the flat background due to the incoherent scattering. After defining the BKG, the difference between $(d\Sigma/d\Omega)_{NUC}$ and BKG, i.e. $I(Q)_{(V,W)C_x}$, is the remaining scattering contribution attributed to the presence of nanoscale $(V,W)C_x$.

To calculate the volume fraction of nanoscale $(V,W)C_x$ f_v, the scattering invariant Q^n [35], a model-independent quantity describing here the area beneath $\left(I(Q)_{(V,W)C_x}\right)Q^2$ vs. Q, was used:

$$Q^n = \int_0^\infty I(Q)_{(V,W)C_x} Q^2 dQ = 2\pi^2(\Delta\rho)^2 f_v(1-f_v) \qquad (1)$$

where $\Delta\rho$, 1.61×10^{-6} $Å^{-2}$, is the average of scattering contrast originated from the nuclear scattering length density difference between $(V,W)C_x$ morphologies and matrix, i.e. Co and WC phases. Q^n values and the volume fraction of nanoscale $(V,W)C_x$ were calculated using SasView software package [36].

VSANS experiments were performed on the double-crystal diffractometer MAUD at LVR15 Reactor, Prague, Czech Republic by using thermal neutrons with wavelength of 2.09 Å at three different instrumental resolutions, resulting in a Q-range of 0.00036–

0.01 $Å^{-1}$. The VSANS patterns were model-fitted in SASproFit software package [37] to determine the average size of Co-rich binder pockets. The details of the VSANS experiments, data treatment, and interpretation can be found in Ref. [28].

2.4. Mean-field simulations

The mean-field simulations were run for the experimentally investigated materials with compositions given in Table 1. The applied model, which is originally developed for plain WC-Co system [38], considers prismatic WC grains with three types of facets (the basal $WC_{(0001)}$/Co and two types of prismatic $WC_{(10\bar{1}0)}$/Co interfaces) and with the characteristic dimensions, corresponding to its height and the distances from the center of the hexagonal basal plane to the two types of prismatic facets (see Supplementary information for details).

The model applied in the present work to simulate the effect of V on the grain size distribution as a function of time is based on the Langer-Swartz-Kampmann-Wagner numerical implementation [38,39]. The initial grain size distribution was the same for all the simulations (see Supplementary Table S1) to be able to rationalize the impact on mobility of the interfaces and changing interfacial energies, both related to V segregation. The equilibrium compositions were determined prior to the simulations using Thermo-Calc Software [40] and TCFE9 Steels/Fe alloys database [41]. No distinction was made between the two types of prismatic $WC_{(10\bar{1}0)}$/Co interfaces. That means prismatic grains were assumed to have a regular hexagonal base. This choice was made to keep a reasonable number of parameters.

During each time step, the system of coarsening rate equations (see Equation (1) in Supplementary information) was solved for every size in the distribution. The volume fraction of the phases and the binder composition were then updated for computing the new chemical driving force and driving force for coarsening using the thermodynamic database [41]. Since three mechanisms, i.e. diffusion, interface friction, and 2D nucleation, are implemented to govern the coarsening of the grains, it was possible to investigate which mechanism is the limiting one depending on the grain size and the material chemistry.

3. Results

3.1. Nanostructure and elemental distributions at the WC/Co interface

Fig. 1 and Fig. 2 represent STEM images of microstructure and EDX analysis at the WC/Co interfaces in the investigated V doped hard metals. Since the equilibrium shape of WC grains is a truncated triangular prism, rectangular-shaped WC grain cross-sections consisting of prismatic $WC_{(10\bar{1}0)}$ and basal $WC_{(0001)}$ habit planes are chosen to study the WC/Co interface chemistry. All rectangular-shaped WC grain cross-sections are viewed along the basal < 0001 > zone axis, confirmed by the selected-area diffraction patterns (SADP) given as an inset in STEM BF images (Fig. 1a and Fig. 2a-d). In Fig. 1b, the $WC_{(0001)}$/Co interface in 0.02% sample is investigated by EDX line profile composition analysis. Interestingly, we find a clear V enrichment within an about 0.4 nm thick interface region shown in Fig. 1c.

In both 0.14% and 0.22% V samples (Fig. 2a and b), the EDX spectral maps reveal more pronounced V enrichment, i.e. $(V,W)C_x$ nano-layers [13,22–24,26], at the $WC_{(0001)}$/Co compared to the $WC_{(10\bar{1}0)}$/Co interface in accordance with [23,25]. The $WC_{(10\bar{1}0)}$/Co interface in the 0.22% V sample is further investigated at higher magnification. The STEM BF image in Fig. 2b3 and the corresponding spectral map indicates the presence of V enrichment at the
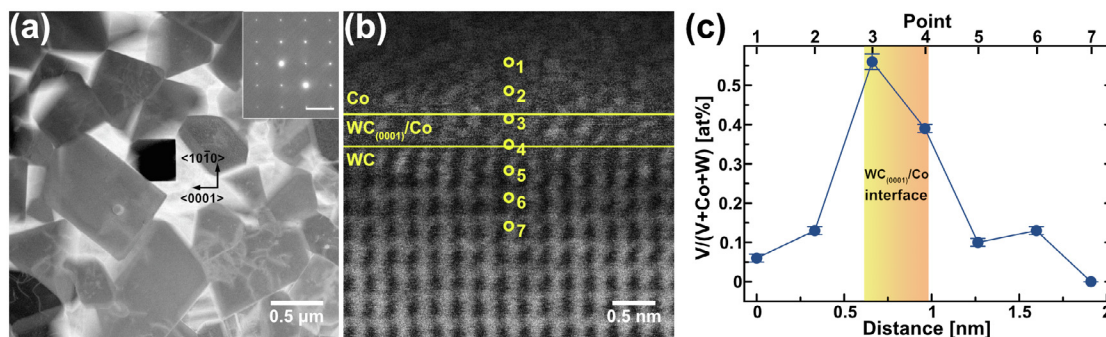
Fig. 1. STEM investigation of nanostructure and EDX analysis of the WC/Co interface in 0.02% V sample. (a) STEM BF image of microstructure, specifying a darker, rectangular-shaped WC grain viewed parallel to the < 0001 > zone axis and its SADP as an inset. Scale bar in SADP corresponds to 5 nm^{-1}. (b) STEM BF image of a $WC_{(0001)}$/Co interface in (a); (c) EDX line profile composition analysis, i.e. V/(V + Co + W) in at%, for points 1 to 7 in (b), revealing a clear V enrichment at the $WC_{(0001)}$/Co interface.

$WC_{(10\bar{1}0)}$/Co interface. When increasing the V addition to 0.39% (Fig. 2c), a few numbers of WC grains with steps at the WC/Co interface are observed. Further increment of V addition (0.76%) results in WC grains with solely stepped WC/Co interface (Fig. 2d). As seen in the STEM BF images of stepped WC/Co interfaces and corresponding spectral maps (Fig. 2c1,2 and Fig. 2d1,2), increasing V addition doesn't seem to cause an enhanced V enrichment at the $WC_{(10\bar{1}0)}$/Co interface. However, it should here be noted that when the electron beam is perpendicular to the $(2\bar{1}\bar{1}0)$ plane of WC grain and parallel to the < 0001 > zone axis, the prismatic plane could end up inclined through the thickness of the thin foil, i.e. not an edge-on condition for the $(10\bar{1}0)$ planar interface. Thus, the WC with $(10\bar{1}0)$ orientation has a variation of thickness at this interface, resulting in diffuse measurements for V atoms. The STEM BF image in Fig. 2d3 represents the near < 0001 > zone axis condition, but having the $(10\bar{1}0)$ interface edge-on. The corresponding spectral map now reveals a comparable V enrichment at the prismatic and basal planes of WC grains. To further quantify the segregation of V and/or formation of nanoscale $(V,W)C_x$ at the WC/Co interfaces, we applied SANS measurements.

3.2. Quantification of nanoscale $(V,W)C_x$

Fig. 3a reveals the evolution of nuclear SANS differential scattering cross-section $(d\Sigma/d\Omega)_{NUC}$ for a probe volume in the mm^3 range, at different amounts of V addition. The reference WC-Co sample, i.e. 0% V, shows the lowest scattering intensity. A deviation from the scattering data of the reference sample is observed upon a small amount (0.022%) of V-doping. Including the high-Q values, ~0.25 Å^{-1}, scattering intensities increased with increasing V addition and reached a maximum in the sample containing 0.766% V. This observation suggests that increasing V content results in a more pronounced scattering contribution from nanoscale features.

Fig. 3b and c depict the scattering contributions of different components in magnetic and nuclear SANS data, respectively, for the sample with 0.76% V. The magnetic SANS patterns and the scattering data from the other samples are given in Supplementary Fig. S1. At the same size range as $(V,W)C_x$ precipitates, the scattering originates mainly from the Co-rich binder. We thus initially use magnetic SANS data to determine the scattering contribution of Co-rich binder pockets $I(Q)_{Co,MAG}$ and later use it in the nuclear scattering pattern to separate scattering contribution of nanoscale $(V,W)C_x$ (see Materials and methods section for details). Finally, after defining the background scattering BKG, the difference between $(d\Sigma/d\Omega)_{NUC}$ and *BKG*, i.e. $I(Q)_{(V,W)C_x}$, in Fig. 3c is the remaining scattering contribution attributed to the presence of

nanoscale $(V,W)C_x$. As can be seen, the scattering contribution of $I(Q)_{(V,W)C_x}$ is visible at the scattering vector Q range > 0.07 Å^{-1}, which corresponds to about < 9 nm in real space, i.e. limited low-Q range and subtraction of BKG ensure that the influence of bulk-scale $(V,W)C_x$ precipitates on analysis is insignificant.

Fig. 3d shows the volume fraction evolution of nanoscale (V,W) C_x as a function of V-addition. As can be seen, the formation of nanoscale $(V,W)C_x$ is clear with an addition of 0.14 wt% V. A slight reduction in the volume fraction is observed in 0.22 wt% V doped sample, but further increments of V addition results in enhanced nanoscale $(V,W)C_x$ formation. The fractions of nanoscale $(V,W)C_x$ reach 0.07 vol% and 0.14 vol% in 0.39 wt% and 0.76 wt% V samples, respectively.

3.3. Evolution of nanoscale $(V,W)C_x$ interfacial layers at solid- and liquid-phase sintering temperatures

The addition of V above the solubility limit of Co can make bulk $(V,W)C_x$ phase thermodynamically stable. Fig. 4 shows the $WC_{(0001)}$/Co interfacial phase diagram, representing the formation of bulk $(V,W)C_x$ phase and nanoscale $(V,W)C_x$ interfacial layers in V doped samples as a function of temperature T and $\Delta\mu_{VC}$. In the case of WC-Co-V system, $\Delta\mu_{VC}$ is the total increment of the chemical potential of V and C needed to surpass the Gibbs energy of VC phase and initiate the formation of bulk $(V,W)C_x$ precipitates [17,19]:

$$\Delta\mu_{VC} = G_{VC} - (\mu_V + \mu_C) \tag{2}$$

where G_{VC} is the Gibbs energy per formula unit of stoichiometric cubic VC; and μ_V and μ_C are the chemical potential per atom of V and C, respectively. We calculated the Gibbs energies and the chemical potentials for the as-sintered sample compositions (Table 1) using Thermo-Calc Software [40] and employing the TCFE9 Steels/ Fe alloys database [41]. The $WC_{(0001)}$/Co interfacial phase diagram comprises three regions: (i) the left region shows the stability range of bulk $(V,W)C_x$ phase with interfacial layers, separated from the middle region by lines representing bulk $(V,W)C_x$ stability for each sample composition; (ii) the middle region represents the high-segregation state, i.e. presence of "*stable*" $(V,W)C_x$ nano-layers, at the $WC_{(0001)}$/Co interface; and, (iii) the right region represents the low segregation state at the $WC_{(0001)}$/Co interface, separated from the high segregation state by a dashed interface transition line calculated by Johansson et al. [19] using density functional theory (DFT) calculations and Monte Carlo simulations. Within the region representing high-segregation state, V content of $(V,W)C_x$ nano-layers decreases towards the interface transition line, i.e. increasing $\Delta\mu_{VC}$. In addition to the ferro- to paramagnetic phase transition,
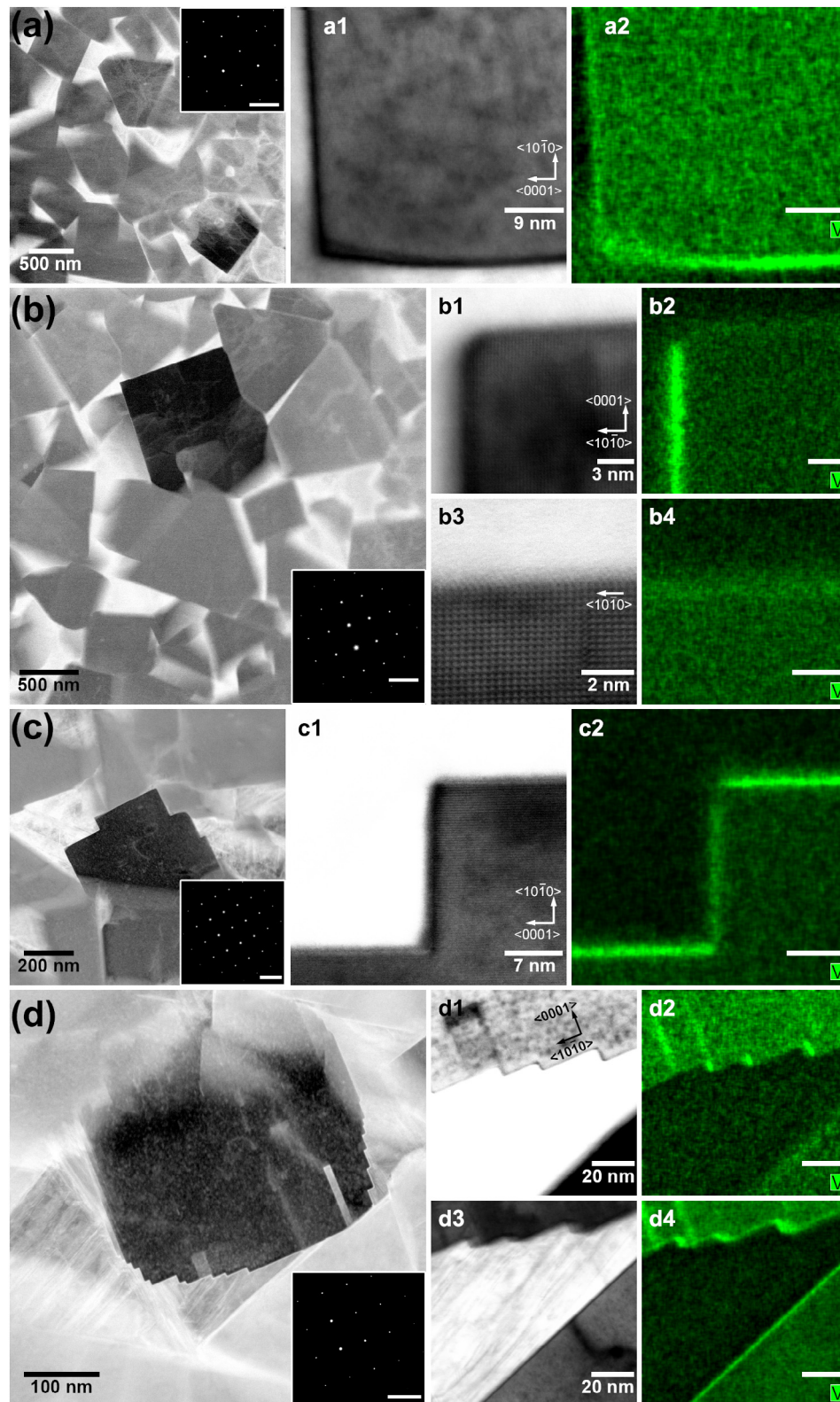
Fig. 2. STEM investigation of nanostructure and EDX analysis of the WC/Co interfaces in 0.14%, 0.22%, 0.39%, and 0.76% V samples. (a-d) STEM BF images of microstructures respectively in 0.14% (a), 0.22% (b), 0.39% (c), and 0.76% V (d) samples. Each image specifies a darker, rectangular-shaped WC grain viewed parallel to the < 0001 > zone axis and its SADP as an inset. Scale bar in SADPs corresponds to 5 nm^{-1}. (a-d1) STEM BF images of a darker, rectangular-shaped WC grains respectively in (a-d), showing the $WC_{(0001)}$/Co and $WC_{(10\bar{1}0)}$/Co interfaces; (a-d2) EDX spectral maps of V respectively for (a-d1). The $WC_{(10\bar{1}0)}$/Co interface in 0.22% V sample is further investigated. (b3) STEM BF image of the $WC_{(10\bar{1}0)}$/Co interface in (b1); (b4) EDX spectral map V for (b3), showing a V segregation also at the $WC_{(10\bar{1}0)}$/Co interface; (d3) STEM BF image of a darker, rectangular-shaped WC grain in (d) acquired in near < 0001 > zone axis condition; (d4) EDX spectral map of V for (d3), revealing now a pronounced V segregation at the WC/ Co interfaces.
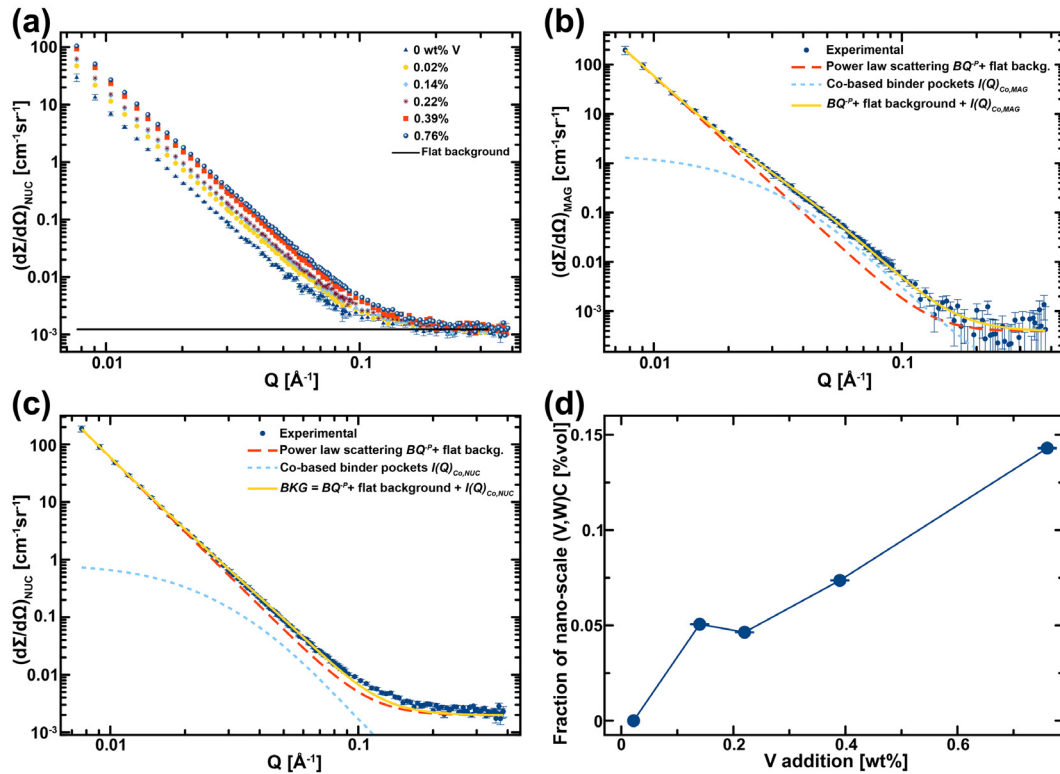
Fig. 3. Quantification of nanoscale $(V,W)C_x$ using SANS. (a) Nuclear SANS patterns of V doped samples, scaled to the same flat background level for a better comparison. Except for 0 wt% V sample, error bars are omitted for clarity as they obscure the data. The error bars on the other data sets are of similar magnitude, as can be asserted from the low scatter of the data points. (b) Magnetic SANS pattern of 0.76 wt% V sample, given together with three scattering contributions. (c) Nuclear SANS pattern of 0.76 wt% V sample. $I(Q)_{Co,NUC}$ is determined from the magnetic SANS pattern. The difference between experimental scattering pattern and *BKG* gives $I(Q)_{(V,W)C_x}$, implying the nanoscale $(V,W)C_x$ morphologies. (d) The volume fraction evolution of nanoscale $(V,W)C_x$ morphologies. The volume fraction uncertainties determined from a fit to the nuclear SANS data are smaller than the symbols.
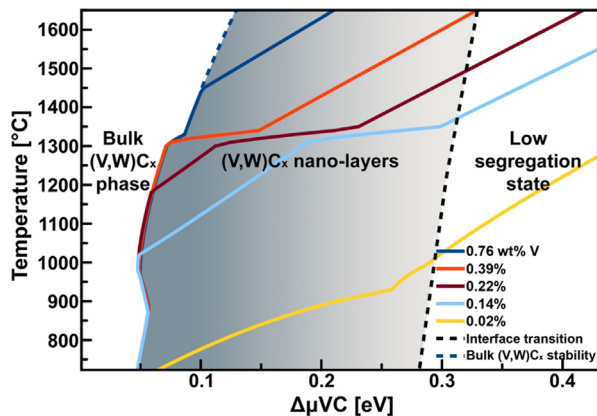

Fig. 4. $WC_{(0001)}$/Co interfacial phase diagram. The dashed blue line is the extension of the bulk $(V,W)C_x$ stability line and valid for V additions above 0.76 wt% with similar C chemical potential. The dashed black line represents the interface transition and is adapted from Ref [19]. In the case of WC-Co-V system, $\Delta\mu_{VC}$ is the total of V and C chemical potential increment needed to initiate the formation of bulk $(V,W)C_x$ precipitates.

solidus and liquidus points of the Co-rich binder, the formation bulk $(V,W)C_x$ phase brings discontinuities to the T vs $\Delta\mu_{VC}$ curves.

Fig. 4 corroborates the presence of $(V,W)C_x$ nano-layers at the $WC_{(0001)}$/Co interface at the solid- and liquid-phase sintering temperatures (with isothermal hold at 1410 °C) for 0.22%, 0.39%, and 0.76% V doped samples. The predictions also suggest that $(V,W)C_x$ nano-layers are present at the $WC_{(0001)}$/Co interfaces in the 0.14% V sample below 1370 °C. The formed layers should grow

during the cooling stage. The formed layers should grow during the cooling stage. This takes place together with the formation of bulk $(V,W)C_x$ precipitates (in 0.22% V sample) and their growth (in samples with $\geq$ 0.22% V) (see Supplementary Fig. S2, where the additional STEM BF microstructure images and corresponding EDX spectral maps show the evolution of bulk $(V,W)C_x$ precipitates). Upon adding 0.76% V, $(V,W)C_x$ nano-layers and bulk precipitates coexist during the isothermal hold at 1410 °C. In 0.02% V sample, on the other hand, we predict only a limited V segregation at the $WC_{(0001)}$/Co interface at a wide range of sintering temperatures, i.e. it is in the low segregation state above 1000 °C. Under equilibrium conditions, the $(V,W)C_x$ nano-layers might form at temperatures below 1000 °C for this composition. However, the applied self-cooling in the furnace leads to a limited diffusion time; thus, we only observed minor V segregations with a thickness of the $WC_{(0001)}$/Co interface of about 0.4 nm as shown in Fig. 1.

3.4. Size evolution of WC grains and Co-rich binder pockets; and mechanical properties

We show in Fig. 5a-f the EBSD maps of WC grains in the hard metals, coloured in accordance with the size of individual WC grains. The microstructures of 0% and 0.02% V samples contain abnormally coarsened WC grains with size reaching in some cases above 5 μm. Even after adding 0.02 wt% V, the hard metals experience an apparent grain coarsening inhibition. Increasing V additions bring even smaller WC grains and this refinement in WC grain size takes place together with hindered abnormal grain coarsening. This finding is supported by the grain area-weighted
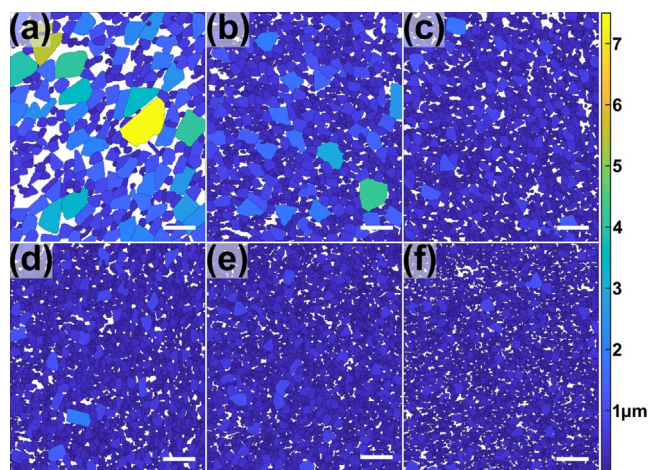
Fig. 5. Coloured EBSD maps of WC grains. (a-f) The colour scheme represents the grain size after sintering in 0%, 0.02%, 0.14%, 0.22%, 0.39%, and 0.76 wt% V samples, respectively. The scale bars represent 2.5 μm. The EBSD data on 0%, 0.02%, 0.22%, and 0.76% V samples were previously presented in Ref. [28].

size distributions of WC grains given in Supplementary Fig. S3, which clearly shows that smaller grains with narrower size distribution are observed with increasing V additions.

In Fig. 6, the impact of V addition on the hardness and the size evolution of WC grains and binder pockets is summarized. The refinement in both WC grains and binder pockets has a linear dependence with respect to V [28]. After a sharp reduction with 0.02% V addition, the average size of WC grains and binder pockets continuously decrease to 301.0 nm and 169.3 nm, respectively, in
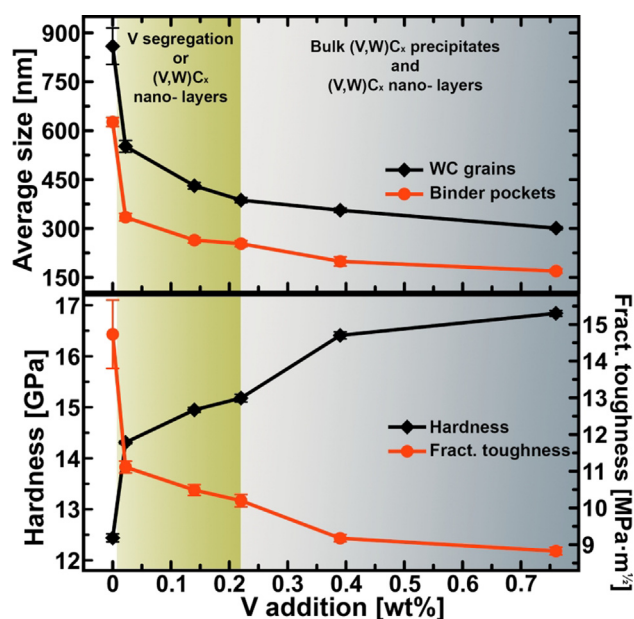

Fig. 6. Evolution of microstructural and mechanical properties as a function of V addition. In the upper section, the WC grain size and Co-rich binder pocket size were determined using EBSD and VSANS, respectively. The uncertainties in the average WC grain size and Co-rich binder pockets values represent the 95% confidence interval calculated according to Ref. [56] and standard deviations from the model fitting, and are typically smaller than the symbols. The EBSD and VSANS data on 0%, 0.02%, 0.22%, and 0.76% V samples were previously presented in Ref. [28]. In the lower section, uncertainties in the hardness and fracture toughness values represent the 95% confidence interval. Information on interface structure, i.e. presence of V segregation or $(V,W)C_x$ nano-layers, and the presence of bulk $(V,W)C_x$ precipitates represent the as-sintered hard materials.

the 0.76% V sample. The hardness of the hard metals increases with the reducing WC grain size [5,6], which takes place at the expense of fracture toughness [42,43]. As shown in Supplementary Fig. S2, upon adding $\geq 0.22\%$ V, the formed bulk $(V,W)C_x$ precipitates appear to have no additional impact on the observed continuous grain coarsening inhibition, but causes brittleness in the WC-Co composite structure. Therefore, the microstructure with optimum hardness and toughness is achieved in the 0.14% V sample, in which both the formation of abnormally large WC grains and bulk $(V,W)C_x$ precipitates are prevented.

4. Discussion

We have shown that V segregation at the WC/Co interfaces starts upon a minor V addition of 0.02 wt% (Fig. 1), resulting in an apparent grain coarsening inhibition with increased hardness and reduced fracture toughness as a consequence, see Fig. 6. Despite the focus on complexions in the literature [13,19,22–24,26], the inhibition effect starting with 0.02% V addition reveals that the grain coarsening inhibition mechanism is not restricted to the presence of *"stable"* $(V,W)C_x$ layers at the WC/Co interfaces. Upon adding 0.14% V, we detect continuous $(V,W)C_x$ nano-layers most notably – but not exclusively – at the $WC_{(0001)}$/Co interfaces (Fig. 2). Whilst EDX spectral maps show a similar level of V segregation at the WC/Co interfaces, the coarsening inhibition becomes more effective with the increasing amounts of V addition. This trend is explained by the SANS results which reveal that the volume fraction of nanoscale $(V,W)C_x$ increases with increasing V addition, suggesting enhanced coverage of nano-layers on WC grains and explaining why similar WC/Co interface structures observed by TEM result in various WC grain size. An exception to this behaviour is the 0.22% V sample, in which the volume fraction of nanoscale $(V,W)C_x$ (0.046%) is similar to that of 0.14% V sample (0.05%). We attribute this similarity to the initiation of bulk $(V,W)C_x$ precipitation that forms during the cooling stage of sintering and competes with the growth of nanoscale $(V,W)C_x$ at the WC/Co interface (see Supplementary Fig. S2). Finally, in 0.76% sample, $(V,W)C_x$ nano-layers present together with bulk precipitates during the isothermal hold at 1410 °C, i.e. the amount of V addition is sufficient enough to saturate the Co-rich binder, resulting in complete coverage on WC grains. Investigations of the WC grain size in 0.88% and 1.12% V samples supports this argument. As seen in Supplementary Fig. S4, increments in V addition above 0.76% bring no notable change in average WC grain size. We can now interrogate the nanostructure evolution and the mechanism of WC grain coarsening inhibition at the solid- and liquid-phase sintering temperatures.

For alloy systems, thermodynamic and kinetic approaches have been pointed out for controlling the grain growth [44–46]. The addition of solute atoms can hinder the growth of grains by reducing: (i) the driving force for grain growth, i.e. thermodynamic stabilization; and, (ii) the grain boundary mobility via impurity drag [47–49] or Zener drag [50–52], i.e. kinetic stabilization. First, the observed presence of V reduces the total interfacial energy of both $WC_{(0001)}$/Co and $WC_{(10\bar{1}0)}$/Co interfaces [25]. Thus, the driving force for Ostwald ripening, i.e. the total driving force for coarsening, is lowered due to its dependence on interfacial energy (see Equation (2) in Supplementary information). This mechanism is valid for all samples, especially those with $\geq 0.22\%$ V additions, having continuous $(V,W)C_x$ layers at the WC/Co interfaces at solid- and liquid-phase sintering temperatures. Second, the presence of V at the WC/Co interfaces in the form of atomic segregation can hinder the motion of WC grain boundaries by the impurity atom drag. Such a drag behaviour has been experimentally validated in Al bicrystals: the activation enthalpy of grain boundary motion

increases with the increasing impurity atom segregation, resulting in a reduced grain boundary mobility [49,53]. A similar drag effect, driven by the atomic segregation of V, contributes to the inhibition of WC grain and binder pocket coarsening in 0.02% and 0.14% V samples. Upon addition of $\geq 0.22\%$ V, we expect the formed *"stable"* $(V,W)C_x$ layers to exert a pinning force, i.e. Zener force, on the moving boundaries. The amount of pinning force increases with the volume fraction of particles attached to the interface [52,53]. Therefore, with an assumption of WC grains covered by similar-sized $(V,W)C_x$ particles, the rise in the volume fraction of nanoscale $(V,W)C_x$ formed at the WC/Co boundary (Fig. 3d) results in increasing pinning forces and reduced interface mobilities, i.e. enhanced kinetic stabilization. Fig. 7 shows schematically the mechanisms of WC grain coarsening inhibition as a function of V addition together with nano- and microstructural evolution, including atomic segregation of V, presence of $(V,W)C_x$ interfacial layers, inhibition of abnormal coarsening of WC grains, formation of stepped WC-Co interface, and formation of $(V,W)C_x$ bulk precipitates.

By running mean-field simulations at the isothermal hold temperature of sintering (1410 °C), in Fig. 8, we show how the mentioned variations in interfacial energy and interface mobility affect the average WC grain size and the total driving force for coarsening. The applied model [38] assumes the same initial WC grain size distribution at the beginning of isothermal hold (see Materials and methods section for details) and uses the adjusted interfacial energies and mobilities of $WC_{(0001)}$/Co and $WC_{(10\bar{1}0)}$/Co interfaces (Table 2) informed by the experimental data and interfacial phase diagram. In 0.02% V sample, in which V atom segregation is observed at $WC_{(0001)}$/Co, only the interfacial energy and interface mobility of $WC_{(0001)}$/Co are lowered. In samples with 0.14% and

0.22% V additions, the interface mobility of $WC_{(0001)}$/Co is gradually reduced with increasing V addition and additional reductions are made in the interface mobility of $WC_{(10\bar{1}0)}$/Co and the interfacial energy of $WC_{(0001)}$/Co. On the other hand, in 0.39% and 0.76% V samples, in which steps at the WC/Co interface and bulk $(V,W)C_x$ precipitates are found, the interfacial energy and interface mobility of $WC_{(10\bar{1}0)}$/Co are reduced. Fig. 8a shows the simulated and the experimentally observed relative average WC grain size values after 1 h of sintering at 1410 °C. For better comparison, both simulated and experimental values are normalized to the average WC grain size in 0% V sample. As can be seen, the mean-field simulations have been able to capture the change in the mean grain size by continuously decreasing the WC/Co interface energies and mobilities, indicating that the interface properties are the governing parameters leading to the grain coarsening inhibition of WC.

In Fig. 8b, we further show for 0% and 0.76% V doped samples as a function of WC grain size the fractions of the total driving force used by the three governing mechanisms that can limit the coarsening of WC grains [7,38]: (i) the diffusion of W and C atoms in the Co-rich binder; (ii) the mobility of $WC_{(0001)}$/Co and $WC_{(10\bar{1}0)}$/Co interfaces; and, (iii) the nucleation of 2D islands of W and C atoms on the WC grain facets. The values represent the 15th minute of the isothermal hold at which a significant difference in WC grain size values is already observed (see inset). In both samples, the diffusion of W and C almost does not consume any driving force; thus, cannot be the limiting mechanism of WC coarsening, it is readily understood since the diffusion in the liquid Co-rich binder at sintering temperatures is very fast. In 0% V sample, the nucleation is the limiting mechanism of grain coarsening, i.e. the mechanism requiring the highest driving force, for smaller WC grains. In
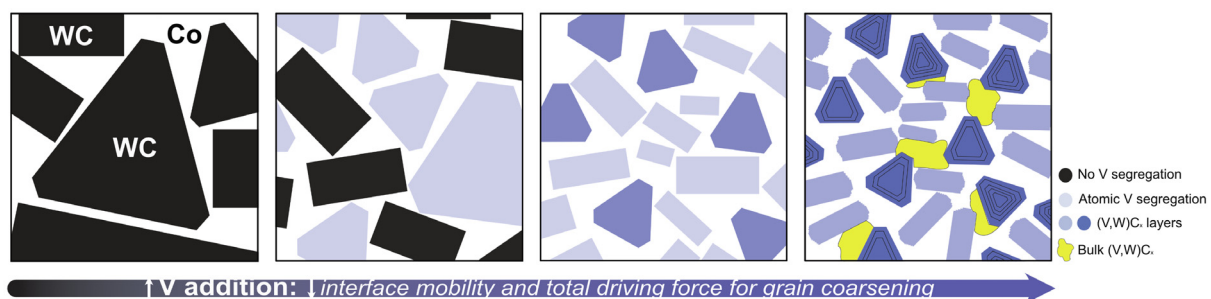

Fig. 7. Schematic illustration. The mechanisms of WC grain coarsening inhibition and structural evolution in V-doped WC-Co hard metals.
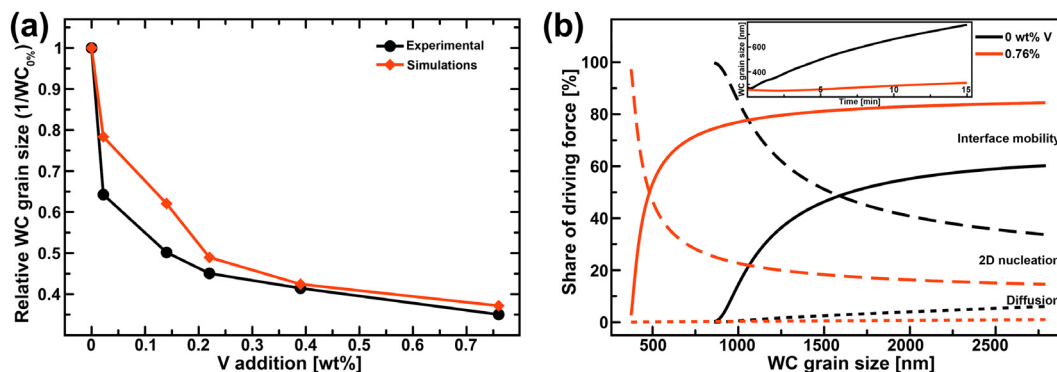

Fig. 8. Mean-field simulations. (a) Modelled and experimentally observed relative average WC grain size values (normalized to the average WC grain size in 0% V sample) after 1 h isothermal hold at 1410 °C. Continuous reduction of the WC/Co interface energies and mobilities with increasing V addition gives smaller WC grain size in simulations, confirming the thermodynamic and kinetic stabilization. (b) Percentages of the driving force used by the diffusion, interface mobility, and 2D nucleation mechanisms in 0% and 0.76% V samples at the 15th minute of the isothermal hold at 1410 °C. The inset shows the WC grain size evolution during the first 15 min.

Table 2
Interface mobilities M and interfacial energies γ of basal b and prismatic p facets used in the mean-field simulations.

wt% V	$M^b(\mathrm{m^4 \cdot J^{-1} \cdot s^{-1}})$	$M^p(\mathrm{m^4 \cdot J^{-1} \cdot s^{-1}})$	$\gamma^b(\mathrm{J.m^{-2}})$	$\gamma^p(\mathrm{J.m^{-2}})$
0	$M_0^b = 3 \times 10^{-15}$	$M_0^p = 5 \times 10^{-15}$	$\gamma_0^b = 1.58$	$\gamma_0^p = 1.81$
0.02	$0.4 \times M_0^b$	M_0^p	$0.85 \times \gamma_0^b$	γ_0^p
0.14	$0.2 \times M_0^b$	$0.7 \times M_0^p$	$0.85 \times \gamma_0^b$	γ_0^p
0.22	$0.1 \times M_0^b$	$0.6 \times M_0^p$	$0.8 \times \gamma_0^b$	γ_0^p
0.39	$0.1 \times M_0^b$	$0.21 \times M_0^p$	$0.8 \times \gamma_0^b$	$0.9 \times \gamma_0^p$
0.76	$0.1 \times M_0^b$	$0.12 \times M_0^p$	$0.8 \times \gamma_0^b$	$0.9 \times \gamma_0^p$

The initial values of M_0^b, M_0^p, γ_0^b, and γ^p representing the un-doped WC-Co system are from Ref. [38].

0.76% V sample, on the other hand, since the WC/Co interface mobility is reduced by the formation of $(V,W)C_x$ interfacial layers, a higher ratio of the driving force is consumed to move the interface, i.e. the interface mobility is the limiting mechanism of the coarsening for a substantially higher proportion of the WC grains. Such a change in the limiting mechanism of coarsening has also an impact on the WC grain morphology. Whilst the perfect flatness of the WC grain facets observed in samples with up to 0.22% V addition is usually associated with the limitation of coarsening by 2D nucleation [54,55], the limiting interface mobility mechanism leads to step formation at the WC/Co interfaces in the materials with additions of 0.39% and 0.76% V (Fig. 2). Once a new nucleus is formed, which is relatively easy compared to the interface movement, it takes a certain time for the new layer to grow laterally as it requires the consumption of a higher part of the driving force. This leads to the simultaneous nucleation of one or a few new layers normal to the grain facet, i.e. step formation.

5. Conclusions

Our present observations provided a comprehensive understanding of WC grain coarsening inhibition in WC-Co hard metals at different V-doping levels. We showed that the atomic segregation of V at the WC/Co interfaces starts upon 0.02 wt% V addition and increasing amounts result in (i) a formation of $(V,W)C_x$ nanolayers at WC/Co interfaces with enhanced coverage on WC grains; and, (ii) the subsequent bulk precipitation of $(V,W)C_x$. The presence of V in terms of atomic segregation and $(V,W)C_x$ nano-layers at the WC/Co interfaces during the sintering (900–1410 °C) brings thermodynamic and kinetic stabilization even above the liquidus temperature of the binder phase. As a consequence, an increasing grain coarsening inhibition effect was observed between 0.02% and 0.76% V additions at which the coverage on WC grains is complete. Thus, further increment in V addition doesn't bring an additional reduction in average WC grain size. By hindering the formation of abnormally large WC grains and brittle bulk $(V,W)C_x$ precipitates, the microstructure with optimum hardness of 15 GPa and fracture toughness of 10.5 MPa·m$^{-1/2}$ was achieved in the 0.14% V sample. The mean-field simulations of WC grain coarsening quantified the proposed coarsening inhibition mechanisms and showed how the small reductions in interface energies and mobilities result in smaller WC grains with stepped WC/Co interface.

CRediT authorship contribution statement

Ahmet Bahadir Yildiz: Conceptualization, Methodology, Formal analysis, Data curation, Writing - original draft. **R. Prasath Babu:** Formal analysis, Data curation, Writing - review & editing. **Manon Bonvalet-Rolland:** Software, Writing - review & editing. **Sebastian Busch:** Formal analysis, Data curation, Writing - review & editing. **Vasyl Ryukhtin:** Formal analysis, Data curation, Writing - review & editing. **Jonathan Weidow:** Formal analysis, Data cura-
tion, Writing - review & editing. **Susanne Norgren:** Resources, Data curation, Writing - review & editing. **Peter Hedström:** Supervision, Conceptualization, Funding acquisition, Writing - review & editing.

Declaration of Competing Interest

The authors declare that they have no known competing financial interests or personal relationships that could have appeared to influence the work reported in this paper.

Data availability

The data that support the findings of this study are available from the corresponding author on request.

Appendix A. Supplementary data

Supplementary data to this article can be found online at https://doi.org/10.1016/j.matdes.2021.109825.

References

[1] Z.Z. Fang, X. Wang, T. Ryu, K.S. Hwang, H.Y. Sohn, Synthesis, sintering, and mechanical properties of nanocrystalline cemented tungsten carbide – A review, Int. J. Refract Metal Hard Mater. 27 (2009) 288–299, https://doi.org/10.1016/j.ijrmhm.2008.07.011.

[2] J. García, V.C. Ciprés, A. Blomqvist, B. Kaplan, Cemented carbide microstructures: a review, Int. J. Refract Metal Hard Mater. 80 (2019) 40–68, https://doi.org/10.1016/j.ijrmhm.2018.12.004.

[3] A. Grearson, M. James, M. Tillman, S. Norgren, P. Gustafson, The future of fine grain hard metals, in: Proc. 16th Int. Plansee Semin. Refract. Hard Mater., Plansee Metall AG, Austria, 2005.

[4] E.O. Hall, Variation of Hardness of Metals with Grain Size, Nature 173 (1954) 948–949, https://doi.org/10.1038/173948b0.

[5] B. Roebuck, Extrapolating hardness-structure property maps in WC/Co hardmetals, Int. J. Refract Metal Hard Mater. 24 (2006) 101–108, https://doi.org/10.1016/J.IJRMHM.2005.04.021.

[6] M. Walbrühl, D. Linder, M. Bonvalet, J. Ågren, A. Borgenstam, ICME guided property design: Room temperature hardness in cemented carbides, Mater. Des. 161 (2019) 35–43, https://doi.org/10.1016/j.matdes.2018.11.029.

[7] K. Mannesson, J. Jeppsson, A. Borgenstam, J. Ågren, Carbide grain growth in cemented carbides, Acta Mater. 59 (2011) 1912–1923, https://doi.org/10.1016/j.actamat.2010.11.056.

[8] I. Borgh, P. Hedström, J. Odqvist, A. Borgenstam, J. Ågren, A. Gholinia, B. Winiarski, P.J. Withers, G.E. Thompson, K. Mingard, M.G. Gee, On the three-dimensional structure of WC grains in cemented carbides, Acta Mater. 61 (2013) 4726–4733, https://doi.org/10.1016/J.ACTAMAT.2013.05.008.

[9] I. Konyashin, 1.15 - Cemented Carbides for Mining, Construction and Wear Parts, in: V.K.B.T.-C.H.M. Sarin (Ed.), Compr. Hard Mater., Elsevier, Oxford, 2014: pp. 425–451. doi:https://doi.org/10.1016/B978-0-08-096527-7.00015-5.

[10] S. Farag, I. Konyashin, B. Ries, The influence of grain growth inhibitors on the microstructure and properties of submicron, ultrafine and nano-structured hardmetals – A review, Int. J. Refract Metal Hard Mater. 77 (2018) 12–30, https://doi.org/10.1016/J.IJRMHM.2018.07.003.

[11] K. Hayashi, Y. Fuke, H. Suzuki, Effects of Addition Carbides on the Grain Size of WC-Co Alloy, J. Japan Soc. Powder Powder Metall. 19 (1972) 67–71, https://doi.org/10.2497/jjspm.19.67.

[12] C.W. Morton, D.J. Wills, K. Stjernberg, The temperature ranges for maximum effectiveness of grain growth inhibitors in WC–Co alloys, Int. J. Refract Metal Hard Mater. 23 (2005) 287–293, https://doi.org/10.1016/j.ijrmhm.2005.05.011.

[13] X. Liu, X. Song, H. Wang, X. Liu, F. Tang, H. Lu, Complexions in WC-Co cemented carbides, Acta Mater. 149 (2018) 164–178, https://doi.org/10.1016/j.actamat.2018.02.018.

[14] B. Wang, Z. Wang, Z. Yin, J. Yuan, J. Jia, Preparation and properties of the VC/Cr3C2/TaC doped ultrafine WC-Co tool material by spark plasma sintering, J. Alloy. Compd. 816 (2020), https://doi.org/10.1016/J.JALLCOM.2019.152598 152598.

[15] M. Baram, D. Chatain, W.D. Kaplan, Nanometer-Thick Equilibrium Films: The Interface Between Thermodynamics and Atomistics, Science (80-.). 332 (2011) 206–209. doi:10.1126/science.1201596.

[16] P.R. Cantwell, M. Tang, S.J. Dillon, J. Luo, G.S. Rohrer, M.P. Harmer, Grain boundary complexions, Acta Mater. 62 (2014) 1–48, https://doi.org/10.1016/j.actamat.2013.07.037.

[17] S.A.E. Johansson, G. Wahnström, First-principles derived complexion diagrams for phase boundaries in doped cemented carbides, Curr. Opin. Solid State Mater. Sci. 20 (2016) 299–307, https://doi.org/10.1016/j.cossms.2016.05.009.

[18] H. Chen, Q. Yang, J. Yang, H. Yang, L. Chen, J. Ruan, Q. Huang, Effects of VC/Cr3C2 on WC grain morphologies and mechanical properties of WC-6wt.%Co cemented carbides, J. Alloy. Compd. 714 (2017) 245–250, https://doi.org/10.1016/J.JALLCOM.2017.04.187.

[19] S.A.E. Johansson, G. Wahnström, First-principles study of an interfacial phase diagram in the V-doped WC-Co system, Phys. Rev. B. 86 (2012) 35403, https://doi.org/10.1103/PhysRevB.86.035403.

[20] J. Weidow, H.-O. Andrén, Grain and phase boundary segregation in WC–Co with small V, Cr or Mn additions, Acta Mater. 58 (2010) 3888–3894, https://doi.org/10.1016/J.ACTAMAT.2010.03.038.

[21] M. Kawakami, O. Terada, K. Hayashi, Effect of Sintering Cooling Rate on V Segregation Amount at WC/Co Interface in VC-doped WC-Co Fine-Grained Hardmetal, J. Japan Soc. Powder Powder Metall. 51 (2004) 576–585, https://doi.org/10.2497/jjspm.51.576.

[22] I. Sugiyama, Y. Mizumukai, T. Taniuchi, K. Okada, F. Shirase, T. Tanase, Y. Ikuhara, T. Yamamoto, Three-dimensional morphology of (W, V)Cx in VC-doped WC–Co hard metals, Scr. Mater. 69 (2013) 473–476, https://doi.org/10.1016/j.scriptamat.2013.06.002.

[23] S. Lay, J. Thibault, S. Hamar-Thibault, Structure and role of the interfacial layers in VC-rich WC-Co cermets, Phil. Mag. 83 (2003) 1175–1190, https://doi.org/10.1080/1478643031000075759.

[24] T. Yamamoto, Y. Ikuhara, T. Sakuma, High resolution transmission electron microscopy study in VC-doped WC–Co compound, Sci. Technol. Adv. Mater. 1 (2000) 97–104, https://doi.org/10.1016/S1468-6996(00)00006-1.

[25] S.A.E. Johansson, G. Wahnström, A computational study of thin cubic carbide films in WC/Co interfaces, Acta Mater. 59 (2011) 171–181, https://doi.org/10.1016/J.ACTAMAT.2010.09.021.

[26] S. Lay, S. Hamar-Thibault, M. Loubradou, Accommodation of the Lattice Mismatch at the VCx-WC Interface, Interface Sci. 12 (2004) 187–195, https://doi.org/10.1023/B:INTS.0000028649.89286.cf.

[27] H. Suzuki, Y. Fuke, K. Hayashi, Grain Size of WC in Sintered WC-VC-Co Alloys, J. Japan Soc. Powder Powder Metall. 19 (1972) 106–112, https://doi.org/10.2497/jjspm.19.106.

[28] A.B. Yildiz, J. Weidow, V. Ryukhtin, S. Norgren, G. Wahnström, P. Hedström, Very-small angle neutron scattering study on grain coarsening inhibition by V-doping of WC-Co composites, Scr. Mater. 173 (2019) 106–109, https://doi.org/10.1016/J.SCRIPTAMAT.2019.08.005.

[29] ASTM B330-15, Standard Test Methods for Estimating Average Particle Size of Metal Powders and Related Compounds Using Air Permeability, ASTM International, West Conshohocken, PA, 2015, https://doi.org/10.1520/B0330-15.

[30] W.D. Schubert, H. Neumeister, G. Kinger, B. Lux, Hardness to toughness relationship of fine-grained WC-Co hardmetals, Int. J. Refract Metal Hard Mater. 16 (1998) 133–142, https://doi.org/10.1016/S0263-4368(98)00028-6.

[31] F. Bachmann, R. Hielscher, H. Schaeben, Grain detection from 2d and 3d EBSD data—Specification of the MTEX algorithm, Ultramicroscopy 111 (2011) 1720–1733, https://doi.org/10.1016/j.ultramic.2011.08.002.

[32] S. Mühlbauer, A. Heinemann, A. Wilhelm, L. Karge, A. Ostermann, I. Defendi, A. Schreyer, W. Petry, R. Gilles, The new small-angle neutron scattering instrument SANS-1 at MLZ—characterization and first results, Nucl. Instruments Methods Phys. Res. Sect. A Accel. Spectrometers, Detect. Assoc. Equip. 832 (2016) 297–305, https://doi.org/10.1016/j.nima.2016.06.105.

[33] U. Keiderling, The new "BerSANS-PC" software for reduction and treatment of small angle neutron scattering data, Appl. Phys. A Mater. Sci. Process. 74 (2002) s1455–s1457, https://doi.org/10.1007/s003390201561.

[34] J. Ilavsky, P.R. Jemian, IUCr, *Irena* : tool suite for modeling and analysis of small-angle scattering, J. Appl. Crystallogr. 42 (2009) 347–353, https://doi.org/10.1107/S0021889809002222.

[35] L.A. Feigin, D.I. Svergun, G.W. Taylor, in: General Principles of Small-Angle Diffraction BT - Structure Analysis by Small-Angle X-Ray and Neutron Scattering, Springer, US, Boston, MA, 1987, pp. 25–55, https://doi.org/10.1007/978-1-4757-6624-0_2.

[36] SasView 5.0.1, http://www.sasview.org/

[37] J. Šaroun, Evaluation of double-crystal SANS data influenced by multiple scattering, J. Appl. Crystallogr. 33 (2000) 824–828, https://doi.org/10.1107/S0021889899013370.

[38] M. Bonvalet, J. Odqvist, J. Ågren, A. Borgenstam, Modelling of prismatic grain growth in cemented carbides, Int. J. Refract Metal Hard Mater. 78 (2019) 310–319, https://doi.org/10.1016/j.ijrmhm.2018.10.007.

[39] J.S. Langer, A.J. Schwartz, Kinetics of nucleation in near-critical fluids, Phys. Rev. A 21 (1980) 948–958, https://doi.org/10.1103/PhysRevA.21.948.

[40] J.O. Andersson, T. Helander, L. Höglund, P. Shi, B. Sundman, Thermo-Calc & DICTRA, computational tools for materials science, CALPHAD: Comput. Coupling Phase Diagrams Thermochem. 26 (2002) 273–312, https://doi.org/10.1016/S0364-5916(02)00037-8.

[41] TCFE9 Steels/Fe-alloys Database, https://www.thermocalc.com/products-services/databases/thermodynamic/tcfe-history/.

[42] W. Jiang, H. Lu, J. Chen, X. Liu, C. Liu, X. Song, Toughening cemented carbides by phase transformation of zirconia, Mater. Des. 202 (2021), https://doi.org/10.1016/j.matdes.2021.109559 109559.

[43] X. Liu, J. Zhang, C. Hou, H. Wang, X. Song, Z. Nie, Mechanisms of WC plastic deformation in cemented carbide, Mater. Des. 150 (2018) 154–164, https://doi.org/10.1016/j.matdes.2018.04.025.

[44] C.C. Koch, R.O. Scattergood, K.A. Darling, J.E. Semones, Stabilization of nanocrystalline grain sizes by solute additions, J. Mater. Sci. 43 (2008) 7264–7272, https://doi.org/10.1007/s10853-008-2870-0.

[45] T. Chookajorn, H.A. Murdoch, C.A. Schuh, Design of Stable Nanocrystalline Alloys, Science (80-.). 337 (2012) 951–954. doi:10.1126/science.1224737.

[46] K. Lu, Stabilizing nanostructures in metals using grain and twin boundary architectures, Nat. Rev. Mater. 1 (2016) 16019, https://doi.org/10.1038/natrevmats.2016.19.

[47] K. Lücke, K. Detert, A quantitative theory of grain-boundary motion and recrystallization in metals in the presence of impurities, Acta Metall. 5 (1957) 628–637, https://doi.org/10.1016/0001-6160(57)90109-8.

[48] J.W. Cahn, The impurity-drag effect in grain boundary motion, Acta Metall. 10 (1962) 789–798, https://doi.org/10.1016/0001-6160(62)90092-5.

[49] D.A. Molodov, U. Czubayko, G. Gottstein, L.S. Shvindlerman, On the effect of purity and orientation on grain boundary motion, Acta Mater. 46 (1998) 553–564, https://doi.org/10.1016/S1359-6454(97)00277-2.

[50] E. Nes, N. Ryum, O. Hunderi, On the Zener drag, Acta Metall. 33 (1985) 11–22, https://doi.org/10.1016/0001-6160(85)90214-7.

[51] C.S. Smith, Grains, Phases, and Interfaces: An Interpretation of Microstructure, Trans. Metall. Soc. AIME. 175 (1948) 15–51.

[52] M. Hillert, Inhibition of grain growth by second-phase particles, Acta Metall. 36 (1988) 3177–3181, https://doi.org/10.1016/0001-6160(88)90053-3.

[53] G. Gottstein, L.S. Shvindlerman, Grain boundary migration in metals: thermodynamics, kinetics, applications, CRC Press, 2009.

[54] W.K. Burton, N. Cabrera, F.C. Frank, N.F. Mott, The growth of crystals and the equilibrium structure of their surfaces, Philos. Trans. R. Soc. London. Ser. A, Math. Phys. Sci. 243 (1951) 299–358. doi:10.1098/rsta.1951.0006.

[55] A.D. Rollett, D.J. Srolovitz, M.P. Anderson, Simulation and theory of abnormal grain growth—anisotropic grain boundary energies and mobilities, Acta Metall. 37 (1989) 1227–1240, https://doi.org/10.1016/0001-6160(89)90117-X.

[56] ASTM E112-13, Standard Test Methods for Determining Average Grain Size, ASTM International, West Conshohocken, PA, 2013, https://doi.org/10.1520/E0112-13.